arXiv:2105.08075v1 [cond-mat.mes-hall] 17 May 2021

Low temperature photo-physics of single NV centers in diamond

Jodok Happacher,[1] David Broadway,[1] Patrick Reiser,[1] Alejandro Jiménez,[2] Märta A. Tschudin,[1] Lucas Thiel,[1] Dominik Rohner,[1] Marcel.li Grimau Puigibert,[1] Brendan Shields,[1] Jeronimo R. Maze,[2] Vincent Jacques,[3] and Patrick Maletinsky[1,*]

[1] *Department of Physics, University of Basel, Klingelbergstrasse 82, Basel CH-4056, Switzerland*
[2] *Facultad de Física, Pontificia Universidad Católica de Chile, Santiago 7820436, Chile*
[3] *Laboratoire Charles Coulomb, Université de Montpellier and CNRS, 34095 Montpellier, France*

(Dated: January 8, 2022)

We investigate the magnetic field dependent photo-physics of individual Nitrogen-Vacancy (NV) color centers in diamond under cryogenic conditions. At distinct magnetic fields, we observe significant reductions in the NV photoluminescence rate, which indicate a marked decrease in the optical readout efficiency of the NV's ground state spin. We assign these dips to excited state level anti-crossings, which occur at magnetic fields that strongly depend on the effective, local strain environment of the NV center. Our results offer new insights into the structure of the NVs' excited states and a new tool for their effective characterization. Using this tool, we observe strong indications for strain-dependent variations of the NV's orbital g-factor, obtain new insights into NV charge state dynamics, and draw important conclusions regarding the applicability of NV centers for low-temperature quantum sensing.

The nitrogen vacancy (NV) lattice defect in diamond [1] hosts a versatile solid state spin system that finds applications in quantum metrology [2], nanoscale imaging [3] or quantum information processing [4]. In these, the NV spin stands out due to its excellent quantum coherence properties, which persist across a wide range of temperatures [5] and pressures [6]. As a result of their performance and robustness, NV spins have been employed in practical applications ranging from remote spin-spin entanglement [7] to nanoscale magnetic imaging [3, 8], even under cryogenic conditions [9, 10].

The majority of such applications build on methods for efficient optical NV spin initialization [11, 12] and readout [13, 14] – two key features that result from properties of the NV's orbital excited states. At temperatures $T \gtrsim 100$ K, orbital averaging allows for a description of the NV excited states as an effective spin-1 system, with spin states $|-1\rangle$, $|0\rangle$, $|1\rangle$, characterized by the magnetic quantum number along the Nitrogen-Vacancy axis [15, 16]. Initialization and readout of the NV's ground-state spin-1 system then result from optical transitions being largely spin-conserving for $|0\rangle$, while excited state spin levels $|\pm1\rangle$ show a non-radiative intersystem crossing into NV spin singlet states, followed by relaxation into the NV triplet ground state [1].

At cryogenic temperatures, however, this effective spin-1 description of the NV excited states does not hold, since orbital averaging slows down and becomes negligible at temperatures $T \lesssim 20$ K [15, 16]. The question how the emerging and rich orbital excited state structure affects the NV's photo-physical properties is of relevance to most low-temperature experiments on NV spins, but has received remarkably little attention thus far. Previous work on NV ensembles has already attributed variations of NV photoluminescence (PL) with magnetic field to mixing of the excited states, but a complete picture was obscured by ensemble averaging [17]. Conversely, for single NVs, only the regime near zero magnetic field and few fixed higher field values have been explored thus far [16, 18]. At the same time, consistent observations of significant reductions in NV PL and spin-readout contrast have been made in the context of low-temperature NV magnetometry [10, 19], but remain unexplained up to now.

To address these questions, we present a systematic study of the photo-physical properties of individual NV centers at cryogenic temperatures. Specifically, we study the dependence of the NV PL rate on static magnetic fields, B_{NV}, applied along the NV axis. We observe significant PL reductions, at well-defined, strain-dependent values of B_{NV}, that we assign to NV excited state level anti-crossings (ESLACs), which result in efficient NV spin mixing and subsequent intersystem crossings. The B_{NV} values where the ESLACs occur further allow for an extraction of the NV's orbital g-factor, g_l. Interestingly, we find previously reported values of g_l to be inconsistent with our observations for NVs experiencing high strain, suggesting a strain dependence of g_l. In addition, our results provide new insights into (i) the mechanisms of NV charge state conversion and (ii) the efficiency of NV spin-initialization and readout, which are valuable for efficient NV-based quantum sensing under cryogenic conditions.

Our experiments are performed using a confocal optical microscope with samples held at temperatures $T \approx 4$ K in a closed-cycle refrigerator with optical access and three-axis vector magnetic field control. Optical excitation is performed with green, continuous-wave laser excitation at power levels close to saturation of the NV's optical transition. For optical detection, we use an avalanche photodiode and appropriate color filters to detect PL predominantly stemming from the NV's negative charge state, NV^-, with corresponding PL photon count rates

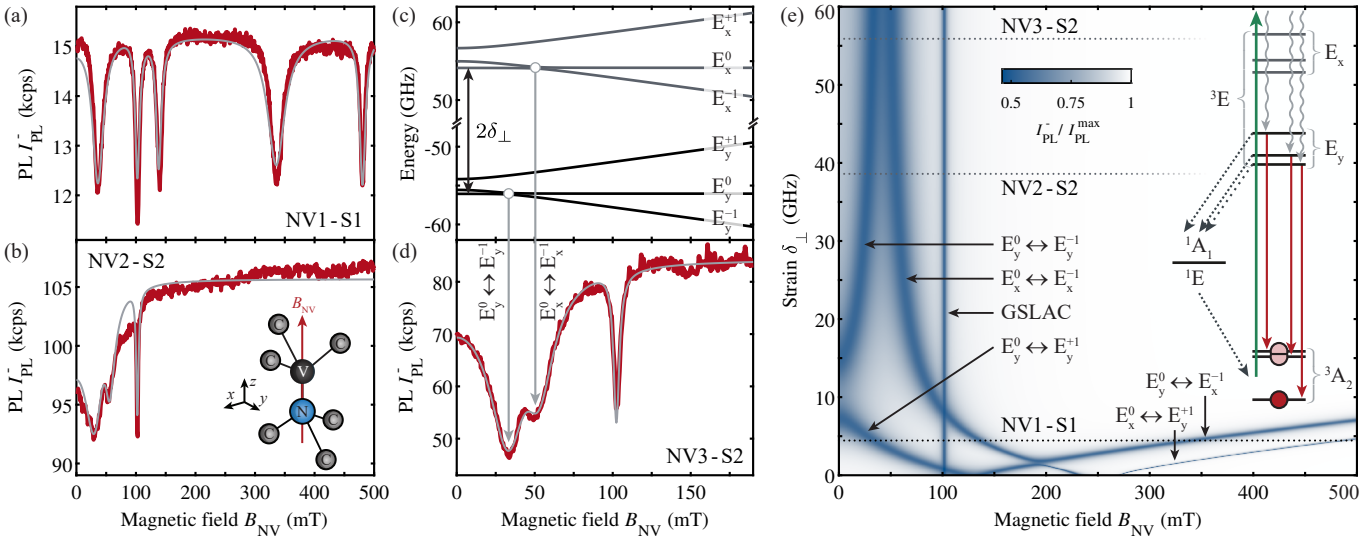


FIG. 1. (a) The NV$^-$ photoluminescence (PL) signal, I_{PL}^-, as a function of magnetic field, B_{NV}, for a typical "low strain" NV, NV1-S1 (transverse strain parameter $\delta_\perp = 4.444(3)$ GHz). (b) Same as (a), but for an NV center exhibiting more strain ($\delta_\perp = 38.6(7)$ GHz). The common I_{PL}^- dip at $B_{NV} = 102.5$ mT in (a) and (b) originates from the well-known ground-state level anti-crossing (GSLAC), while additional dips result from excited-state level anti-crossings (ESLACs). Grey lines are fits to our model (see text and [20]). All data were recorded at a temperature $T \approx 4$ K. (c) Example of NV$^-$ excited state energies for an NV experiencing even higher strain ($\delta_\perp = 55.9$ GHz). Labels indicate the orbital- and spin degree of freedom of the states. (d) B_{NV} dependence of I_{PL}^- for NV3-S2 with $\delta_\perp = 55.9(6)$ GHz. The vertical arrows assign the observed I_{PL}^- dips to the corresponding ESLACs shown in (c). (e) PL intensity I_{PL}^- as a function of B_{NV} and $\delta_\perp$, calculated from a classical rate equation model for the 10-level system illustrated in (e) (for details see [20]). Labels in (e) indicate which ESLACs are responsible for the respective PL dips, while horizontal lines show the $\delta_\perp$-values for the NVs presented in panels (a), (b), and (d). Inset: Electronic levels and transition pathways considered in simulating the magnetic field dependence of I_{PL}^-. The NV$^-$ excited state energies are illustrated for the limit of large strain.

I_{PL}^-.

We first investigate individual NV centers in two (100)−oriented, single-crystal "electronic grade" diamonds (Element-Six), grown by chemical vapour deposition. These two samples differ in the nature of their NVs: In sample S1, we study naturally occurring NV centers, several microns deep in the bulk, while in sample S2, ~ 10 nm deep NVs have been created by $^{14}N^+$ ion implantation at 12 keV and subsequent annealing. These two types of NV defects were chosen for studying a broad range of local strain, which is known to be increased for NVs implanted close to the diamond surface [21]. To enhance NV PL collection efficiencies, diamond solid immersion lenses and nanopillars were structured on samples S1 and S2, respectively, with methods reported elsewhere [22–24].

Figures 1a and b show representative data of I_{PL}^- as a function of B_{NV}, for two NV centers, NV1-S1 and NV2-S2 (where NVk-Sl denotes the k-th NV located in sample Sl). For both NVs, $I_{PL}^-(B_{NV})$ shows several distinct, narrow local minima ("dips") at specific values of B_{NV}. The prominent, narrow dip at $B_{NV} = 102.5$ mT results from the NV's well-known ground-state level anti-crossing (GSLAC) [25] and is present for all NVs we investigated. Conversely, the multiple additional dips, which occur reproducibly for each NV, only at different values of B_{NV}, are thus far unaccounted for.

We attribute the observed I_{PL}^- dips (excluding the GSLAC) to ESLACs, which result in spin mixing and subsequent population shelving into the NV$^-$ singlet manifold. Figures 1c, d exemplify this concept for NV3-S2, where we show calculated NV$^-$ excited state energies [1, 16, 26] (described below) alongside a measurement of $I_{PL}^-(B_{NV})$ to illustrate the coalescence between two ESLACs and the associated I_{PL}^- dips.

To obtain further, quantitative insights, we employ an extended version of a classical rate-equation model of the NV's magnetic field-dependent photo-physics [12, 17], where we now explicitly take into account the full, low-temperature excited state level structure of NV$^-$ [26] (see Fig. 1e, inset, for the electronic states and population decay channels taken into account). For our calculations, we fix all transition rates to literature values by Gupta et al. [27][28], and only leave the relevant parameters of the NV$^-$ excited state Hamiltonian as free variables.

The energy splittings of the NV$^-$ excited states sensitively depend on lattice strain transverse to the NV axis. Such strain can result from electric fields or crystal stress [26], which we combine into a single perpendicular strain parameter $\delta_\perp = \sqrt{\delta_x^2 + \delta_y^2}$, where $\delta_{x(y)}$ are the corresponding strain parameters along x and y (Fig. 1b,

inset). We then calculate the NV ^3E state energies by the Hamiltonian [1]

$$\hat{H}_{ES} = \hat{H}_{FS} + \delta_x\hat{\sigma}_z + \delta_y\hat{\sigma}_x + \mu_B(g_l\hat{\sigma}_y + g_e\hat{S}_z)B_{\mathrm{NV}}, \quad (1)$$

where $\hat{H}_{FS}$ is the fine structure Hamiltonian of the ^3E manifold [1], $\hat{\sigma}_i$ are the Pauli matrices representing the excited state orbital operators in the basis $\{E_x, E_y\}$ (the eigenstates of $\hat{H}_{ES}$ in the limit $\delta_\perp \gg ||\hat{H}_{FS}||$), $\hat{S}_z$ is the $S = 1$ spin operator along the z-axis, $\mu_B = 28$ GHz/T is the Bohr magneton and $g_{l(e)}$ is the orbital (electron) g-factor ($g_e = 2.01$ [1]). Figure 1e shows the resulting model prediction of $I^-_{\mathrm{PL}}(B_{\mathrm{NV}})$ for varying $\delta_\perp$, and shows the strong dependence of the various I^-_{PL} dip locations on $\delta_\perp$. This explains the strongly varying $I^-_{\mathrm{PL}}(B_{\mathrm{NV}})$ traces we observe between different NVs, which naturally experience different levels of $\delta_\perp$. Conversely, a measurement of $I^-_{\mathrm{PL}}(B_{\mathrm{NV}})$ offers a sensitive tool to determine $\delta_\perp$ on the level of single NVs – a task that otherwise requires complex spectroscopic techniques [16].

We use our model to fit all $I^-_{\mathrm{PL}}(B_{\mathrm{NV}})$ data presented in this work, where grey lines overlaid on data show the resulting fits. For the fits we only left $\delta_\perp$, and a small misalignment angle in B_{NV} (and g_l in the case of NV1-S1 – see below) as free parameters in Hamiltonian (1). In addition, we allow for scaling constants for contrast and normalization of I^-_{PL} and a parameter describing the relative excitation efficiency into orbitals E_x and E_y [15] to vary. All resulting fit parameters with errors are reported in [20]. We note that despite these few degrees of freedom, our model yields excellent fits for NVs experiencing a large range of strain-values, from $\delta_\perp \lesssim ||\hat{H}_{FS}||$ (Fig. 1a) to $\delta_\perp \gg ||\hat{H}_{FS}||$ (Fig. 1b).

However, we observe significant deviations when studying $I^-_{\mathrm{PL}}(B_{\mathrm{NV}})$ for more highly strained NVs at elevated magnetic fields. There, our model predicts two additional I^-_{PL} dips (labelled $E^0_{x(y)} \leftrightarrow E^{\pm1}_{y(x)}$ in Fig. 1e), which arise from spin-mixing ESLACs between orbitals E_x and E_y. To experimentally address this regime, we investigate single NV defects hosted in the (111)−oriented, electronic grade diamond S3 [29]. Figure 2a shows low-field $I^-_{\mathrm{PL}}(B_{\mathrm{NV}})$ data for the representative NV4-S3, where a fit (light blue) yields $\delta_\perp = 42.3(5)$ GHz [20], for which our model predicts the $E^0_{x(y)} \leftrightarrow E^{\pm1}_{y(x)}$ dips to occur at Tesla-range magnetic fields (Fig. 2b, light blue). Importantly, the $E^0_{x(y)} \leftrightarrow E^{\pm1}_{y(x)}$ dip location depends sensitively on g_l (blue traces in Fig. 2b and Fig. 2c), while the locations of the "low-field" I^-_{PL} dips shown in Fig. 2a are largely independent of g_l (Fig. 2d). Conversely, an observation of the $E_{x(y)} \leftrightarrow E_{y(x)}$ LACs yields a sensitive determination of g_l on the level of single NVs. For NV4-S3 or any other NV we studied in sample S3, we were unable to observe the $E^0_{x(y)} \leftrightarrow E^{\pm1}_{y(x)}$ ESLACs, despite extensive experimental efforts; an observation which could be explained by an unexpected increase of g_l. Specifically, for the $\delta_\perp$ value of NV4-S3, $g_l \approx 0.8$ is the lowest value

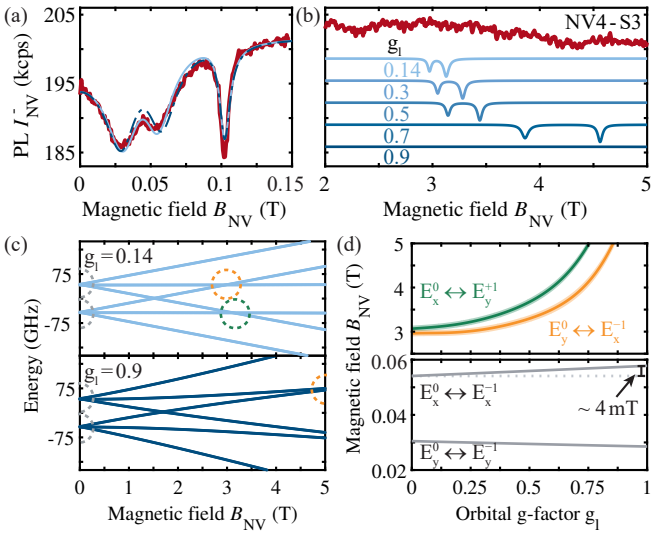


FIG. 2. (a) $I^-_{\mathrm{PL}}(B_{\mathrm{NV}})$ data (red) for NV4-S3 in the "low-field" regime ($B_{\mathrm{NV}} \lesssim 150$ mT). The model fit (blue) yields $\delta_\perp = 42.3(5)$ GHz and is largely unaffected by the value of g_l ($g_l = 0.14...0.9$; light to dark blue). (b) Same as (a) for stronger magnetic fields. Blue-shaded curves show model predictions (vertically offset for clarity) for $\delta_\perp = 42.3$ GHz and $g_l = 0.14...0.9$ (see labels). (c) Calculated ^3E excited state energies for $g_l = 0.14$ and $g_l = 0.9$. Dashed circles highlight the position of the $E_{x(y)} \leftrightarrow E_{y(x)}$ (green) and $E_{x(y)} \leftrightarrow E_{x(y)}$ (gray) ESLACs. (d) g_l-dependence of the B_{NV} values at which various ESLACs occur. Shaded areas correspond to the propagated fitting errors in $\delta_\perp$ from (a).

consistent with our observations (Fig. 2d), and we find similar conclusions for ∼ 10 further NVs with comparable values of $\delta_\perp$, where we examined $I^-_{\mathrm{PL}}(B_{\mathrm{NV}})$ for B_{NV} up to 5 T [20].

Our observations thus suggest a surprising, strain-induced enhancement of the orbital g-factor of NV$^-$ over reported literature values $g_l \approx 0.1...0.22$ [17, 30–32]. Such an effect has not been discussed in literature thus far, but can be made plausible by qualitative arguments. At low strain, the NV's orbital excited states are near-degenerate, which allows for Jahn-Teller coupling to lead to a reduction of orbital angular momentum [31, 33]. With increasing strain, the energy splitting of the states increases, which suppresses Jahn-Teller mixing, and thereby restores orbital angular momentum, leading to an increase of g_l towards the classical value $g_l = 1$. While a complete theoretical description of this suggested g_l enhancement is still lacking and beyond the scope of this work, we expect our findings to trigger further theoretical work on the topic.

Our method of monitoring I^-_{PL} versus B_{NV} also offers insights into the charge dynamics of the NV center. Specifically, we conducted experiments where we chose appropriate color filters [20] to record the PL intensity I^0_{PL} from the neutral charge state, NV^0 (Fig. 3a,b). Strikingly, we find that all previously described I^-_{PL} dips are

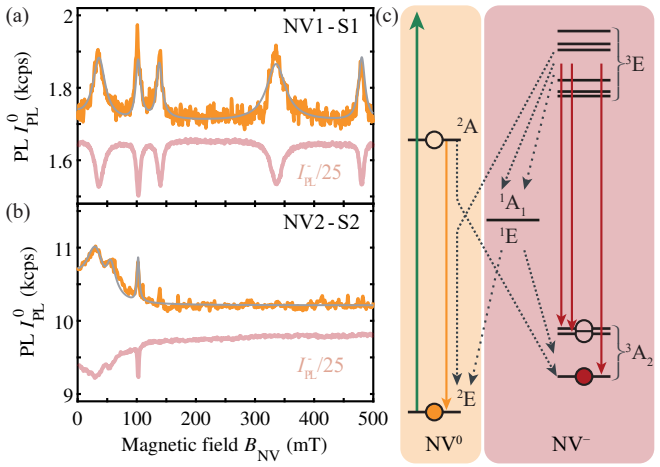


FIG. 3. (a) Magnetic field dependence of the NV^0 PL rate, $I^0_{PL}(B_{NV})$, for NV1-S1 and (b) NV2-S2, along with the corresponding I^-_{PL}-data (gray data-points taken from Fig. 1a,b, but rescaled for clarity). Gray lines are theory predictions based on the fits shown in Fig. 1a,b. (c) Electronic states of the NV^0-NV$^-$ system, with corresponding (de-)ionization rates, used to include charge-state dynamics into the model introduced in Fig. 1f.

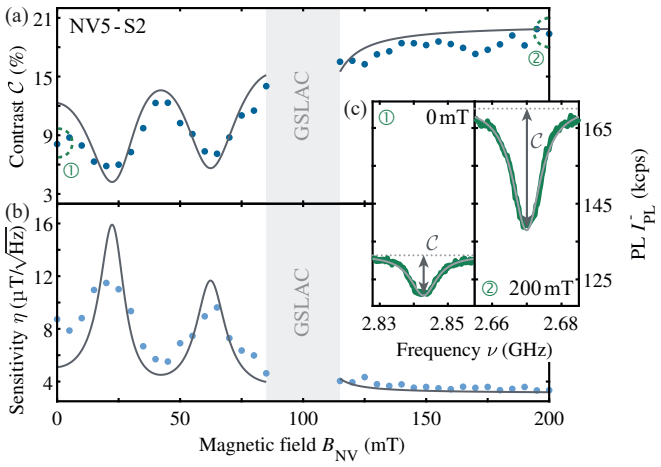


FIG. 4. (a) Dependence of the optically detected magnetic resonance (ODMR) contrast on magnetic field B_{NV} for NV5-S2. The microwave field amplitude (Rabi frequency) was held constant while varying B_{NV}. (b) Magnetic field dependence of the magnetic field sensitivity extracted from data (see text). Dark grey lines in a and b show theory predictions based on independently recorded $I^-_{PL}(B_{NV})$ data (see [20]). (c) Exemplary ODMR traces recorded at values of B_{NV} (dotted circles in (a)), where magnetic field sensitivity is maximally (left) and minimally (right) affected by excited state level anticrossings.

mirrored by peaks in I^0_{PL}. While the resulting buildup of NV^0 population remains small (and therefore only minimally affects our conclusions thus far), our model can be extended to include previously reported NV$^0 \leftrightarrow$NV$^-$ (de)ionization processes [34, 35] (Fig. 3c). Importantly, within our model we can only explain the observed I^0_{PL} peaks by including a recently proposed [34], decay channel from the NV$^-$ singlet state ^1E to the ground state of NV^0 – without this process our model yields dips instead of peaks in I^0_{PL}. Using the previously measured (de)ionization rates [34, 35], our model then yields a quantitative prediction for $I^0_{PL}(B_{NV})$, without any free fit parameters, other than scaling constants for contrast and normalization of I^0_{PL} (grey lines in Fig. 3a,b).

The ESLAC induced dips in I^-_{PL} also have important implications for the magnetic-field sensitivity in low-temperature NV magnetometry. Indeed, the dips in I^-_{PL} are accompanied by corresponding dips in the spin readout contrast $\mathcal{C}$ of optically detected magnetic resonance (ODMR) [36]. Figure 4a shows the evolution $\mathcal{C}(B_{NV})$ for NV5-S2, while two exemplary ODMR traces recorded at and away from an I^-_{PL} dip ($B_{NV} = 0$ and 200 mT, respectively) are shown in Fig. 4c. This combined reduction in I^-_{PL} and $\mathcal{C}$ severely affect the NV's magnetic field sensitivity η. Using the well-established estimate [13, 37] $\eta = \frac{4}{3\sqrt{3}} \frac{\Delta\nu}{\gamma_{NV}\mathcal{C}\sqrt{I^-_{PL}}}$, where $\Delta\nu$ is the ODMR linewidth, and $\gamma_{NV} = 28$ GHz/T the NV's gyromagnetic ratio, we extract $\eta(B_{NV})$ shown in Fig. 4b. Compared to typical sensitivity values $\eta \approx 3\ \mu\text{T}/\text{Hz}^{0.5}$ away from the ESLACs (e.g. at $B_{NV} \approx 200$ mT), η drops by almost an order of magnitude on the I^-_{PL} dips.

For nanoscale NV magnetometry, which exploits near-surface NV centers for which we consistently find $\delta_\perp >$ 20 GHz (Fig. 1f), this decrease of magnetometry performance predominantly affects magnetometry at $B_{NV} \lesssim$ 100 mT (c.f. Fig. 1f). The fact that all such "shallow" NVs exhibit significant values of $\delta_\perp$ can be assigned to internal electric fields due to band bending near the diamond surface [21, 38], or to near-surface crystal stress [39]. Magnetic field sensitivity for such NVs could in the future be restored by materials engineering to reduce $\delta_\perp$ near diamond surfaces, by working with NVs oriented normal to the diamond surface [40] or by harnessing the dependence of the I^-_{PL} dip depth on the excitation laser polarization [15, 20]. Further improvements could be achieved by optimising laser excitation powers or by exploiting resonant laser excitation where specific ESLACs could be avoided by choosing the proper laser excitation frequency.

Our work on the low temperature magnetic field dependence of NV fluorescence rates offers a simple, yet precise and quantitative tool to characterize the excited state structure of individual NV centers. These findings not only offer insights into the NV center orbital structure and charge dynamics, but are also relevant to applications in quantum information processing and quantum sensing, where precise knowledge of the excited state structure is key. Exploring the temperature-dependence of the I^-_{PL} dips would constitute a worthwhile extension to our work that might offer further insights into orbital averaging processes that dominate the NV's photo-

physics at elevated temperatures [15]. Importantly, the method we demonstrated and applied here is not limited to NV centers alone – the excited state structure of any colour center exhibiting dark states that can be populated through magnetic field tunable ESLACs, such as the neutral Silicon-Vacancy center in diamond [41], could be investigated as well.

We gratefully acknowledge Ronald Hanson, Arian Stolk and their colleagues for making sample S1 available for this study and Johannes Kölbl for help in creating the figures. We further acknowledge financial support through the NCCR QSIT (Grant No. 185902), the Swiss Nanoscience Institute, the EU Quantum Flagship Project ASTERIQS (Grant No. 820394), and through the Swiss NSF Project Grant No. 188521.

* patrick.maletinksy@unibas.ch

[1] M. W. Doherty, N. B. Manson, P. Delaney, F. Jelezko, J. Wrachtrup, and L. C. L. Hollenberg, Physics Reports **528**, 1 (2013).
[2] C. L. Degen, F. Reinhard, and P. Cappellaro, Reviews of Modern Physics **89**, 035002 (2017).
[3] F. Casola, T. van der Sar, and A. Yacoby, Nature Reviews Materials **3**, 17088 (2018).
[4] N. Kalb, A. A. Reiserer, P. C. Humphreys, J. J. W. Bakermans, S. J. Kamerling, N. H. Nickerson, S. C. Benjamin, D. J. Twitchen, M. Markham, and R. Hanson, Science **356**, 928 (2017).
[5] D. M. Toyli, D. J. Christle, A. Alkauskas, B. B. Buckley, C. G. Van de Walle, and D. D. Awschalom, Physical Review X **2**, 031001 (2012).
[6] K.-M. C. Fu, G. Z. Iwata, A. Wickenbrock, and D. Budker, AVS Quantum Science **2**, 044702 (2020).
[7] B. Hensen, H. Bernien, A. E. Dreau, A. Reiserer, N. Kalb, M. S. Blok, J. Ruitenberg, R. F. L. Vermeulen, R. N. Schouten, C. Abellan, W. Amaya, V. Pruneri, M. W. Mitchell, M. Markham, D. J. Twitchen, D. Elkouss, S. Wehner, T. H. Taminiau, and R. Hanson, Nature **526**, 682 (2015).
[8] L. Rondin, J.-P. Tetienne, T. Hingant, J.-F. Roch, P. Maletinsky, and V. Jacques, Reports Prog. Phys. **77**, 056503 (2014).
[9] L. Thiel, D. Rohner, M. Ganzhorn, P. Appel, E. Neu, B. Müller, R. Kleiner, D. Koelle, and P. Maletinsky, Nature Nanotechnology **11**, 677 (2016).
[10] L. Thiel, Z. Wang, M. A. Tschudin, D. Rohner, I. Gutierrez-Lezama, N. Ubrig, M. Gibertini, E. Giannini, A. F. Morpurgo, and P. Maletinsky, Science **364**, 973 (2019).
[11] J. Harrison, M. J. Sellars, and N. B. Manson, J. Lumin. **107**, 245 (2004).
[12] J.-P. Tetienne, L. Rondin, P. Spinicelli, M. Chipaux, T. Debuisschert, J.-F. Roch, and V. Jacques, New J. Phys. **14**, 103033 (2012).
[13] A. Dréau, M. Lesik, L. Rondin, P. Spinicelli, O. Arcizet, J. F. Roch, and V. Jacques, Phys. Rev. B - Condens. Matter Mater. Phys. **84**, 1 (2011).
[14] M. Steiner, P. Neumann, J. Beck, F. Jelezko, and J. Wrachtrup, Phys. Rev. B **81**, 1 (2010).
[15] K. M. C. Fu, C. Santori, P. E. Barclay, L. J. Rogers, N. B. Manson, and R. G. Beausoleil, Phys. Rev. Lett. **103**, 256404 (2009).
[16] A. Batalov, V. Jacques, F. Kaiser, P. Siyushev, P. Neumann, L. J. Rogers, R. L. McMurtrie, N. B. Manson, F. Jelezko, and J. Wrachtrup, Physical Review Letters **102**, 195506 (2009).
[17] L. J. Rogers, R. L. McMurtrie, M. J. Sellars, and N. B. Manson, New Journal of Physics **11**, 063007 (2009).
[18] M. Pompili, S. L. Hermans, S. Baier, H. K. Beukers, P. C. Humphreys, R. N. Schouten, R. F. Vermeulen, M. J. Tiggelman, L. dos Santos Martins, B. Dirkse, *et al.*, Science **372**, 259 (2021).
[19] S. E. Lillie, D. A. Broadway, N. Dontschuk, S. C. Scholten, B. C. Johnson, S. Wolf, S. Rachel, L. C. L. Hollenberg, and J.-P. Tetienne, Nano Lett. **20**, 1855 (2020).
[20] "supplementary online information,".
[21] D. A. Broadway, N. Dontschuk, A. Tsai, S. E. Lillie, C. T.-K. Lew, J. C. McCallum, B. C. Johnson, M. W. Doherty, A. Stacey, L. C. L. Hollenberg, and J.-P. Tetienne, Nat. Electron. **1**, 502 (2018).
[22] N. Hedrich, D. Rohner, M. Batzer, P. Maletinsky, and B. J. Shields, Phys. Rev. Applied **14**, 064007 (2020).
[23] L. Robledo, L. Childress, H. Bernien, B. Hensen, P. F. A. Alkemade, and R. Hanson, Nature **477**, 574 (2011).
[24] E. Neu, P. Appel, M. Ganzhorn, J. Miguel-Sánchez, M. Lesik, V. Mille, V. Jacques, A. Tallaire, J. Achard, and P. Maletinsky, Applied Physics Letters **104**, 153108 (2014).
[25] A. Wickenbrock, H. Zheng, L. Bougas, N. Leefer, S. Afach, A. Jarmola, V. M. Acosta, and D. Budker, Applied Physics Letters **109**, 053505 (2016).
[26] J. R. Maze, A. Gali, E. Togan, Y. Chu, A. Trifonov, E. Kaxiras, and M. D. Lukin, New J. Phys. **13**, 025025 (2011).
[27] A. Gupta, L. Hacquebard, and L. Childress, JOSA B **33**, B28 (2016).
[28] We note that our main findings are insensitive to the rates employed and we find largely identical results by employing other literature values.
[29] E. Neu, P. Appel, M. Ganzhorn, J. Miguel-Sánchez, M. Lesik, V. Mille, V. Jacques, A. Tallaire, J. Achard, and P. Maletinsky, Applied Physics Letters **104** (2014).
[30] N. Reddy, N. Manson, and E. Krausz, Journal of Luminescence **38**, 46 (1987).
[31] D. Braukmann, E. R. Glaser, T. A. Kennedy, M. Bayer, and J. Debus, Phys. Rev. B **97**, 195448 (2018).
[32] H. Hanzawa, H. Nishikori, Y. Nisida, S. Sato, T. Nakashima, S. Sasaki, and N. Miura, Physica B: Condensed Matter **184**, 137 (1993).
[33] D. Braukmann, *Optical properties of vacancies in diamond at high magnetic elds*, Ph.D. thesis, TU Dortmund University, Germany (2018).
[34] D. Aude Craik, P. Kehayias, A. Greenspon, X. Zhang, M. Turner, J. Schloss, E. Bauch, C. Hart, E. Hu, and R. Walsworth, Phys. Rev. Applied **14**, 014009 (2020).
[35] N. Aslam, G. Waldherr, P. Neumann, F. Jelezko, and J. Wrachtrup, New J. Phys. **15**, 013064 (2013).
[36] A. Gruber, A. Drabenstedt, C. Tietz, L. Fleury, J. Wrachtrup, and C. Borczyskowski, Science **276**, 2012 (1997).
[37] J. F. Barry, J. M. Schloss, E. Bauch, M. J. Turner, C. A. Hart, L. M. Pham, and R. L. Walsworth, Rev. Mod.

Phys. **92**, 015004 (2019).
[38] A. Stacey, N. Dontschuk, J.-P. Chou, D. A. Broadway, A. K. Schenk, M. J. Sear, J.-P. Tetienne, A. Hoffman, S. Prawer, C. I. Pakes, A. Tadich, N. P. de Leon, A. Gali, and L. C. L. Hollenberg, Adv. Mater. Interfaces **6**, 1801449 (2019).
[39] D. J. McCloskey, N. Dontschuk, D. A. Broadway, A. Nadarajah, A. Stacey, J. P. Tetienne, L. C. Hollenberg, S. Prawer, and D. A. Simpson, ACS Appl. Mater. Interfaces **12**, 13421 (2020).
[40] D. Rohner, J. Happacher, P. Reiser, M. A. Tschudin, A. Tallaire, J. Achard, B. J. Shields, and P. Maletinsky, Applied Physics Letters **115**, 192401 (2019).
[41] Z.-H. Zhang, P. Stevenson, G. m. H. Thiering, B. C. Rose, D. Huang, A. M. Edmonds, M. L. Markham, S. A. Lyon, A. Gali, and N. P. de Leon, Phys. Rev. Lett. **125**, 237402 (2020).
[42] M. L. Goldman, M. W. Doherty, A. Sipahigil, N. Y. Yao, S. D. Bennett, N. B. Manson, A. Kubanek, and M. D. Lukin, Physical Review B **91**, 165201 (2015).
[43] L. Robledo, H. Bernien, T. van der Sar, and R. Hanson, New Journal of Physics **13**, 025013 (2011).
[44] P. Appel, E. Neu, M. Ganzhorn, A. Barfuss, M. Batzer, M. Gratz, A. Tschöpe, and P. Maletinsky, Review of Scientific Instruments **87**, 063703 (2016), http://aip.scitation.org/doi/pdf/10.1063/1.4952953.
[45] A. Tallaire, J. Achard, A. Boussadi, O. Brinza, A. Gicquel, I. Kupriyanov, Y. Palyanov, G. Sakr, and J. Barjon, Diamond and Related Materials **41**, 34 (2014).
[46] M. Lesik, J.-P. Tetienne, A. Tallaire, J. Achard, V. Mille, A. Gicquel, J.-F. Roch, and V. Jacques, ArXiv e-prints (2014), arXiv:1401.2795.
[47] K. J. Brown, E. Chartier, E. M. Sweet, D. A. Hopper, and L. C. Bassett, Journal of Chemical Health and Safety **26**, 40 (2019).
[48] V. Jacques, P. Neumann, J. Beck, M. Markham, D. Twitchen, J. Meijer, F. Kaiser, G. Balasubramanian, F. Jelezko, and J. Wrachtrup, Phys. Rev. Lett. **102**, 057403 (2009).

SUPPLEMENTARY INFORMATION

CONTENTS

References 5

Supplementary Information 7

Theoretical description 7
NV spin Hamiltonians 7
Transition rate equations 8
Extension of rate equation model to include NV^0 11

Description of fitting methods 12
Magnetic field dependent photoluminescence of the NV^- 12
Magnetic field dependent photoluminescence of the two NV charge states 12

Experimental details 15
Experimental apparatus 15
Samples details 16
g_l factor measurements 17
Magnetic field sensitivity 18
Polarization dependence of the NV PL 18

Theoretical description

NV spin Hamiltonians

To obtain further, quantitative insights, into the photo-physics of NV centers at low temperature we employ an extended version of a classical rate-equation model of the NV's magnetic-field dependent photo-physics [12, 17], which explicitly takes into account the low-temperature excited state structure of NV^- [26].

For an appropriate description of the NV photo-dynamics at low temperatures one needs to consider both the ground and excited states Hamiltonians. Here we describe the model using the Hamiltonian previously described by Doherty et al [1] but this process can also be performed using the alternative Hamiltonian form described by Maze et al [26].

The canonical spin-Hamiltonian of the NV spin's ground state Hamiltonian is

$$\hat{\mathcal{H}}_{gs} = D_{gs}\Big[\hat{S}_z^2 - S(S+1)/3\ \mathbb{1}_3\Big], \tag{2}$$

where $D_{gs} \approx 2.88\ GHz$, $S = 1$ for a spin 1 system, $\hat{S}_z$ is the spin operator and $\mathbb{1}_3$ is the identity matrix. The NV spin's internal hyperfine coupling and quadrupole moment are neglected as we observed no additional effect from these terms.

The NV spin's ground state level structure is further modified by static electric ($\vec{E}$), magnetic ($\vec{B}$) and strain ($\vec{\delta}$) fields, whose contribution is given by

$$\begin{aligned}\hat{\mathcal{V}}_{gs} = {} & \mu_B g_{gs}^{\parallel}\hat{S}_z B_z + \mu_B g_{gs}^{\perp}\Big(\hat{S}_x B_x + \hat{S}_y B_y\Big) + d_{gs}^{\parallel}(E_z+\delta_z)\Big[\hat{S}_z^2 - S(S+1)/3\ \mathbb{1}_3\Big] \\ & + d_{gs}^{\perp}(E_x+\delta_x)\Big(\hat{S}_y^2 - \hat{S}_x^2\Big) + d_{gs}^{\perp}(E_y+\delta_y)\Big(\hat{S}_x\hat{S}_y + \hat{S}_y\hat{S}_x\Big),\end{aligned} \tag{3}$$

where μ_B is the Bohr magnetron, $g_{gs}^{\parallel}$ and $g_{gs}^{\perp}$ are the components of the ground state electronic g-factor tensor, $d_{gs}^{\parallel}$ and $d_{gs}^{\perp}$ are the components of the ground state electric dipole moment. The electric field and reduced stress tensor terms are treated as a single effective electric field.

The excited state of the nitrogen vacancy is an orbital doublet whose nature is masked at higher temperatures due to an orbital averaging. The low temperature fine structure of the NV spin is given by the effective Hamiltonian,

$$\begin{aligned}\hat{\mathcal{H}}_{es} = & \mathbb{1}_2 \otimes D_{es}^{\parallel}\Big[\hat{S}_z^2 - S(S+1)/3\ \mathbb{1}_3\Big] \\ & - \lambda_{es}^{\parallel}\ \hat{\sigma}_y \otimes \hat{S}_z + D_{es}^{\perp}\Big[\hat{\sigma}_z \otimes \Big(\hat{S}_y^2 - \hat{S}_x^2\Big) - \hat{\sigma}_x \otimes \Big(\hat{S}_x\hat{S}_y + \hat{S}_y\hat{S}_x\Big)\Big] \\ & + \lambda_{es}^{\perp}\Big[\hat{\sigma}_z \otimes \Big(\hat{S}_x\hat{S}_z + \hat{S}_z\hat{S}_x\Big) - \hat{\sigma}_x \otimes \Big(\hat{S}_y\hat{S}_z + \hat{S}_z\hat{S}_y\Big)\Big],\end{aligned} \tag{4}$$

where $\sigma_{x,y,z}$ is the standard two level Pauli spin matrices, $D_{es}^{\parallel}$ and $D_{es}^{\perp}$ are the spin-spin interaction terms, and $\lambda_{es}^{\parallel}$ and $\lambda_{es}^{\perp}$ are spin-orbit interaction terms. This excited state Hamiltonian results in two spin-1 systems, one for each of the two orbital branches.

The influence of external field on the NV spin's excited states level structure is given by,

$$\begin{aligned}\hat{\mathcal{V}}_{es}^{LT} = & d_{es}^{\parallel}\Big(E_z + \delta_z\Big)\ \mathbb{1}_2 \otimes \mathbb{1}_3 + d_{es}^{\perp}\Big(E_x + \delta_x\Big)\ \hat{\sigma}_z \otimes \mathbb{1}_3 - d_{es}^{\perp}\Big(E_y + \delta_y\Big)\ \sigma_x \otimes \mathbb{1}_3 \\ & + \mu_B\ l_{es}^{\parallel}\ B_z\ \hat{\sigma}_y \otimes \mathbb{1}_3 + \mathbb{1}_2 \otimes \mu_B\ g_{es}^{\parallel}\ B_z\ \hat{S}_z + \mu_B\ g_{es}^{\perp}\Big(B_x\hat{S}_z + B_y\hat{S}_y\Big)\end{aligned} \tag{5}$$

where $d_{es}^{\parallel}$ and $d_{es}^{\perp}$ are components of the electronic dipole moment, $l_{es}^{\parallel}$ is the orbital magnetic moment also referred as g_l, the effective orbital g-factor and $g_{es}^{\parallel}$ and $g_{es}^{\perp}$ are components of the electronic g-factor tensor.

Transition rate equations

For an appropriate description of the photo-dynamics of a single NV at low temperatures one needs to consider the interplay between the three levels in the ground state, the six levels in the two orbital branches of the excited state and the metastable singlet. The singlet can be reduced to one state with rates in and out of it [42], leaving ten states. We employ an extended version of a classical rate-equation model of the NV's magnetic-field dependent photo-physics [12, 17].

The states for the rate equation are defined as:
Ground state:

$$\begin{aligned}|1\rangle &\equiv {}^3A_2^0 \\ |2\rangle &\equiv {}^3A_2^{-1} \\ |3\rangle &\equiv {}^3A_2^{+1}\end{aligned}$$

Excited state:

$$\begin{aligned}|4\rangle &\equiv {}^3E_y^0 \\ |5\rangle &\equiv {}^3E_y^{-1} \\ |6\rangle &\equiv {}^3E_y^{+1} \\ |7\rangle &\equiv {}^3E_x^0 \\ |8\rangle &\equiv {}^3E_x^{-1} \\ |9\rangle &\equiv {}^3E_x^{+1}\end{aligned}$$

Combined singlet state:

$$|10\rangle \equiv {}^1A_1/{}^1E$$

Where the Eigenstates are give in the same notation as the main text. Which is X^{m_s}, where X including the pre superscript and post subscript denote the orbital branch and the post subscript m_s denotes the spin level, e.g. $E_y^{-1} \equiv |E_y, -1\rangle = |\text{orbital state}, \text{spin state}\rangle$.

The NV^- can be optically excited with a green laser through a dipole-allowed transition to the excited state, which is a spin conserving. This excitation does have a polarization-dependence, which is due to selection rules. However,

this dependence is suppressed due to the non-radiative decay observed from the non-resonant optical excitation [15], leading to a small effect on the populations in the two excited state orbital-branches. Once in the excited state manifold, the NV spin can decay back to the ground state through two different decay channel: a radiative and an non-radiative decay. The radiative decay is directly from the excited state back to the ground state. While the non-radiative decay path is through the inter-system crossing (ISC) to a metastable singlet state, where a difference in the rates from the $m_s = 0$ versus $m_s = \pm 1$ spin states is observed [12].

We begin with transition rates between ground- and excited-states with zero external field, i.e. where the spin quantum number is still well defined. Where these rates have been experientially measured [12, 23, 27]. The basis of the transition matrix are the ten eigenvectors $\left|i^0\right\rangle$ with $i = 1, ..., 10.$ labeled with subscript ^{0} indicating that this is the basis at zero field.

In the following we make the assumption that spin conserving relaxation rates from the excited to ground states are the same for each spin state and that the non-spin conserving transitions are zero. The non-spin conserving transitions rates have previously been shown to only be a few percent compared to the spin-conserving one [23].

The zero-field pumping rate can be assumed to be the respective relaxation rates from the excited state to the ground state k_r (where the r stands for radiative) multiplied by a pumping parameter β which is proportional to laser power. To capture the polarization dependence of the excitation we separate this pumping parameter into one for each orbital state β_{E_x} and β_{E_y}. The transition rates from the ground to excited states are thus defined as

$$\begin{aligned} k^0_{|1^0\rangle\to|4^0\rangle} &= \beta_{E_y}\, k_r & \qquad k^0_{|1^0\rangle\to|7^0\rangle} &= \beta_{E_x}\, k_r \\ k^0_{|2^0\rangle\to|5^0\rangle} &= \beta_{E_y}\, k_r & \qquad k^0_{|2^0\rangle\to|8^0\rangle} &= \beta_{E_x}\, k_r \\ k^0_{|3^0\rangle\to|6^0\rangle} &= \beta_{E_y}\, k_r & \qquad k^0_{|3^0\rangle\to|9^0\rangle} &= \beta_{E_x}\, k_r \end{aligned} \tag{6}$$

where the direct radiative decay transition rates from the excited to ground states are define as

$$\begin{aligned} k^0_{|4^0\rangle\to|1^0\rangle} &= k_r & \qquad k^0_{|7^0\rangle\to|1^0\rangle} &= k_r \\ k^0_{|5^0\rangle\to|2^0\rangle} &= k_r & \qquad k^0_{|8^0\rangle\to|2^0\rangle} &= k_r \\ k^0_{|6^0\rangle\to|3^0\rangle} &= k_r & \qquad k^0_{|9^0\rangle\to|3^0\rangle} &= k_r \end{aligned} \tag{7}$$

The transition rates from the excited states to the metastable state are spin dependent and defined as

$$\begin{aligned} k^0_{|4^0\rangle\to|10^0\rangle} &= k_{nr_0} & \qquad k^0_{|7^0\rangle\to|10^0\rangle} &= k_{nr_0} \\ k^0_{|5^0\rangle\to|10^0\rangle} &= k_{nr_{\pm 1}} & \qquad k^0_{|8^0\rangle\to|10^0\rangle} &= k_{nr_{\pm 1}} \\ k^0_{|6^0\rangle\to|10^0\rangle} &= k_{nr_{\pm 1}} & \qquad k^0_{|9^0\rangle\to|10^0\rangle} &= k_{nr_{\pm 1}} \end{aligned} \tag{8}$$

where $k_{nr_0} \ll k_{nr_{\pm 1}}$ [12].

The rates from the metastable state to the ground states are similar for all spin states and defined as,

$$\begin{aligned} k^0_{|10^0\rangle\to|1^0\rangle} &= k_{m_0} \\ k^0_{|10^0\rangle\to|2^0\rangle} &= k_{m_{\pm 1}} \\ k^0_{|10^0\rangle\to|3^0\rangle} &= k_{m_{\pm 1}} \end{aligned} \tag{9}$$

where $k_{m_0} \sim k_{m_{\pm 1}}$.

In a typical optically detected magnetic resonance (ODMR) measurement the spin population is transferred between the spin states of the ground state via an applied microwave field, and are defined as

$$\begin{aligned} k^0_{|1^0\rangle\to|2\rangle^0} &= k^0_{|2^0\rangle\to|1^0\rangle} = k_{MW_{-1}} \\ k^0_{|1^0\rangle\to|3\rangle^0} &= k^0_{|3^0\rangle\to|1^0\rangle} = k_{MW_1} \end{aligned} \tag{10}$$

where k_{MW_x} is the driving transition rate on resonance with the x transition between the $|0\rangle$ and $|x\rangle$ states. These rates are only non-zero when modeling the effect of the level anti crossings on ODMR in the main text.

All these transition rates have been measured experimentally, shown in Table . In the model we used the parameters from Gupta et al. [27], which we found the best agreement with our data.

Reference	k_r	k_{nr_0}	k_{nr_1}	k_{m_0}	$k_{m_{\pm1}}$
Robledo et al. [43]	65	11	80	3.0	2.6
Tetienne et al. [12]	65.9	7.9	53.3	0.98	0.73
Gupta et al. [27]	66.8	10.5	90.7	4.8	2.2

TABLE I. Experimentally measured transition rates at zero field. All of the rates are in MHz.

We can now define the transition rate matrix at zero-field in this 10-level model. The transition matrix, Q^0, gives the rates at zero electric, magnetic and strain field and is defined as

$$Q^0 = \begin{pmatrix} 0 & k_{MW_{-1}} & k_{MW_1} & \beta_{E_x}\, k_r & 0 & 0 & \beta_{E_y}\, k_r & 0 & 0 & 0 \\ k_{MW_{-1}} & 0 & 0 & 0 & \beta_{E_x}\, k_r & 0 & 0 & \beta_{E_y}\, k_r & 0 & 0 \\ k_{MW_1} & 0 & 0 & 0 & 0 & \beta_{E_x}\, k_r & 0 & 0 & \beta_{E_y}\, k_r & 0 \\ k_r & 0 & 0 & 0 & 0 & 0 & 0 & 0 & 0 & k_{nr_0} \\ 0 & k_r & 0 & 0 & 0 & 0 & 0 & 0 & 0 & k_{nr_{\pm1}} \\ 0 & 0 & k_r & 0 & 0 & 0 & 0 & 0 & 0 & k_{nr_{\pm1}} \\ k_r & 0 & 0 & 0 & 0 & 0 & 0 & 0 & 0 & k_{nr_0} \\ 0 & k_r & 0 & 0 & 0 & 0 & 0 & 0 & 0 & k_{nr_{\pm1}} \\ 0 & 0 & k_r & 0 & 0 & 0 & 0 & 0 & 0 & k_{nr_{\pm1}} \\ k_{m_0} & k_{m_{\pm1}} & k_{m_{\pm1}} & 0 & 0 & 0 & 0 & 0 & 0 & 0 \end{pmatrix}. \tag{11}$$

This zero field transition matrix is extend to arbitrary fields by calculating the spin-state overlap. Since the new eigenstates are a linear combination of the previous eigenstates the scalar product is used to evaluate the corresponding overlap,

$$|i\rangle = \sum_{j=1}^{10} \alpha_{ij} \left|j^0\right\rangle \tag{12}$$

where α_{ij} is the projection of the new state $|i\rangle$ onto the zero-field basis states $|j\rangle$. This resulting transition matrix which depends on the magnetic field $\boldsymbol{B}$, the electric field $\boldsymbol{E}$ and the stress field $\boldsymbol{\delta}$ is:

$$Q(\boldsymbol{B}, \boldsymbol{E}, \boldsymbol{\delta})_{ij} = \sum_{k=1}^{10} \sum_{l=1}^{10} \alpha_{ik}^2 Q_{kl}^0 \alpha_{jl}^2. \tag{13}$$

With this transition matrix a classical rate equation for the system can be defined where N_i is the population in each state and $\boldsymbol{M}$ is the rate equation matrix. We assume that this is a closed loop system, which impose the inclusion of diagonal terms such that,

$$M_{ij} = \begin{cases} \sum_{k=1}^{10} -Q_{ik} & \text{if } i = j \\ Q_{ji} & \text{if } i \neq j \end{cases} \tag{14}$$

The rate equation problem is stated in the following equation:

$$\frac{dN_i}{dt} = \boldsymbol{M} N_i \tag{15}$$

Where the populations in the steady state is given by the smallest eigenvalue and is normalised such that

$$\hat{N}_i = \frac{N_i}{\sum_{j=1}^{10} N_j}. \tag{16}$$

The photoluminescence of the NV^-, I_{PL}^-, is calculated by summing over the relevant radiative transitions from the excited state to the ground state and populations of these states, such that

$$I_{\mathrm{PL}}^- = \sum_{i=4,5,6} \sum_{j=1}^{3} Q_{ij} \hat{N}_i + \sum_{i=7,8,9} \sum_{j=1}^{3} Q_{ij} \hat{N}_i. \tag{17}$$

Additional modification to the photoluminescence such as background fluorescence, $I_{\rm bck}$, and collection efficiency, $\eta_{\rm collection}$, can also be introduced, such that

$$I^-_{\rm PL} \equiv I^-_{\rm Total} = \eta_{\rm collection} I^-_{\rm PL} + I_{\rm bck}. \tag{18}$$

The ODMR contrast $\mathcal{C}$ is calculated by the photoluminescence $I^-_P L$ with and without a driving field in the grounds state. For example, with a microwave driving between $|1\rangle$ ($^3A^0_2$) and $|2\rangle$ ($^3A^{-1}_2$), the contrast can be determined by calculating,

$$\mathcal{C} = \frac{I^-_{\rm PL}(k_{MW_{-1}} = 0) - I^-_{\rm PL}(k_{MW_{-1}} \neq 0)}{I_{\rm PL}(k_{MW_{-1}} = 0)} \tag{19}$$

Extension of rate equation model to include NV^0

To account for possible charge state change between NV$^-$ and NV^0 we extend the model to include the energy levels of the NV^0 as well as transition rates between the two charge states. The NV^0 consists of two eigenstates, one ground state $|11\rangle$ and an excited state $|12\rangle$:

$$|11\rangle \equiv {}^2E$$
$$|12\rangle \equiv {}^2A$$

The transition within the NV^0 charge state and between the two charge states are defined as follows:

From the excited state of the NV^0 there is a direct radiative decay down to the NV^0 ground state:

$$k_{|12^0\rangle \to |11^0\rangle} = k_{r_{NV^0}} \tag{20}$$

The transition rate from the ground state to the excited state of the NV^0 is defined as the product of the radiative transition rate and the pumping power β_{NV^0}, such that

$$k_{|11^0\rangle \to |12^0\rangle} = \beta\, k_{r_{NV^0}}. \tag{21}$$

The recombination rate from the NV^0 excited state to the NV$^-$ ground state is given by

$$\begin{aligned} k_{|12^0\rangle \to |1^0\rangle} &= k_{\rm recomb} \\ k_{|12^0\rangle \to |2^0\rangle} &= k_{\rm recomb} \\ k_{|12^0\rangle \to |3^0\rangle} &= k_{\rm recomb} \end{aligned} \tag{22}$$

The ionization rate from the NV$^-$ excited state to the NV^0 ground state is given by

$$\begin{aligned} k_{|4^0\rangle \to |11^0\rangle} &= k_{\rm ion} & k_{|7^0\rangle \to |11^0\rangle} &= k_{\rm ion} \\ k_{|5^0\rangle \to |11^0\rangle} &= k_{\rm ion} & k_{|8^0\rangle \to |11^0\rangle} &= k_{\rm ion} \\ k_{|6^0\rangle \to |11^0\rangle} &= k_{\rm ion} & k_{|9^0\rangle \to |11^0\rangle} &= k_{\rm ion} \end{aligned} \tag{23}$$

The recombination rate and ionization rate in the dark between the ground state of the NV^0 and the ground state of the NV$^-$.

$$\begin{aligned} k_{|1^0\rangle \to |11^0\rangle} &= k_{\rm darkion} & k_{|11^0\rangle \to |1^0\rangle} &= k_{\rm darkrecomb} \\ k_{|2^0\rangle \to |11^0\rangle} &= k_{\rm darkion} & k_{|11^0\rangle \to |2^0\rangle} &= k_{\rm darkrecomb} \\ k_{|3^0\rangle \to |11^0\rangle} &= k_{\rm darkion} & k_{|11^0\rangle \to |3^0\rangle} &= k_{\rm darkrecomb} \end{aligned} \tag{24}$$

where for continuous wave excitation the dark ionization and recombination rates are effective zero, $k_{\rm darkrecomb} = k_{\rm darkion} = 0$.

Additionally, we include a newly postulated shelf ionization transition [34] which goes from the metastable state to the NV^0 ground state and is laser driven:

$$k_{|10^0\rangle \to |11^0\rangle} = k_{\rm shelfion} \tag{25}$$

The rates for these charges state from the literature adapted to our nomenclature are found in Table .

The photoluminescence, $I^0_{\rm PL}$, is calculated by looking at the population and the transition rate of the radiative transition of the NV^0. The rates are given by the corresponding transition matrix $Q(\boldsymbol{B}, \boldsymbol{E}, \boldsymbol{\delta})_{ij}$.

$$I^0_{\rm PL} = Q_{11,\,12}\, \hat{N}_{12} \tag{26}$$

Where both background counts and collection efficiency can be included in the same fashion as in the NV$^-$.

Reference	$k_{r_{NV^0}}$	k_{ion}	k_{recomb}	k_{shelfion}	k_{darkion}	$k_{\text{darkrecomb}}$
Craik, et al. [34]	50	$0.037\beta k_r$	$0.8\beta k_r$	$0.36\beta k_r$	100	300

TABLE II. Experimentally measured transition rates for the NV^0 and the transitions between NV^0 and NV^-. All of the rates are in MHz.

NV-Sample	$\delta_\perp$ (GHz)	ϕ_δ (°)	g_l	θ_B (°)	β_{E_x}	β_{E_y}	I^-_{bck} (cps)
NV1-S1	4.444(3)	-11.6(1.3)	0.1395(9)	1.14(3)	0.0221(3)	0.0242(5)	4378(92)
NV2-S2	38.6(7)	1(59)	(fixed to 0.14)	0.61(3)	0.085(5)	0.186(14)	70910(244)
NV3-S2	55.9(6)	-32.2(6)	(fixed to 0.14)	0.502(10)	0.240(6)	0.64(2)	9091(231)
NV5-S2	32.0(5)	-29(3)	(fixed to 0.14)	0.20(2)	0.43(3)	0.52(5)	83198(883)
NV4-S3	42.3(5)	-26(2)	(fixed to 0.14)	1.06(3)	0.102(3)	0.164(7)	158011(234)

TABLE III. Summary of the fit results of the I^-_{PL} spectra.

Description of fitting methods

Magnetic field dependent photoluminescence of the NV^-

Using the model described in Section , we fit the PL spectra as a function of magnetic field, using the rates from Ref. [27]. In general, the model is over constrained and as a consequence requires some approximations in order to fit accurately and physically. The full model would include 14 parameters: three magnetic field components, three electric field components, three stress parameters (shear stress is ignored), two pumping rates, the collection efficiency, the background counts, and the effective g-factor. We treat the combination of the electric field and the stress as one effective stress field, reducing the six corresponding parameters to three. Furthermore, the positions of the ESLACs are independent of the z-component of the effective strain parameter, which is thus disregarded from the fit. We parametrize the magnetic field in spherical coordinates, with the tilt angle of the magnetic field away from the NV quantization axis denoted as θ_B. In our experiments, the magnetic field alignment is such that $\theta_B \sim 0$, in which case the azimuthal angle ϕ_B of the magnetic field has no significant effect on the NV excited state spectrum and we set $\phi_B = 0$. Finally, we define the photon collection efficiency η to be constant and identical to all NVs and set $\eta = 0.005$. This leaves the fit with only 8 parameters, such that:

$$I^-_{\text{PL}} = f(B_{NV}, \theta_B, \delta_\perp, \phi_\delta, \beta_{E_x}, \beta_{E_y}, I_{\text{bck}}, g_l) \tag{27}$$

where $\delta_\perp = \sqrt{\delta_x^2 + \delta_y^2}$ and ϕ_δ is an angle such that $\delta_x = \delta_\perp \sin(\phi_\delta)$ and $\delta_y = \delta_\perp \cos(\phi_\delta)$.

As discussed in the main text, the effective g-factor, g_l, can only be confidently determined in the low stress regime. We thus let g_l vary as a free fit parameter for NV1-S1 only, but keep this parameter fixes for all NVs with more elevated strain values. There, we set $g_l = 0.14$ – the value determined on NV1-S1. As we argue in the main text, g_l varies with strain, and fixing g_l for these NVs might therefore introduce certain systematic errors in our fits. However, as illustrated in Fig.2d (lower panel), the magnetic field values at which the $E^0_{x(y)} \leftrightarrow E^{-1}_{x(y)}$ ESLACs occur, depend only very weakly on the value of g_l and we therefore consider these errors to be close to negligible.

All of the fit results are summarized in Table. , and the fits from the NV's mentioned in the main text are shown in Figures 5 to 9.

Magnetic field dependent photoluminescence of the two NV charge states

The NV^0 PL can be fitted with the above presented 12-level model including the NV^0 ground and excited states. The physical parameters for the NV (θ_B, $\delta_\perp$, ϕ_δ, β_{E_x}, β_{E_y}) which have been extracted from the fit to the corresponding NV^- PL data, are used as constant parameters in the model and are not fitted. As a pumping parameter for the NV^0 and the laser power dependent shelf-ionization rate from the singlet we take the average between the two pumping parameters to the two NV^- ES orbitals.

The only free parameters left are scaling parameters such that:

$$I^0_{\text{PL}} = f(\eta_{NV^0}, I^0_{\text{bck}}) \tag{28}$$

where η_{NV^0} is the collection efficiency for the NV^0 PL and I^0_{bck} are the background counts in the wavelength spectrum of the collected NV^0 PL.

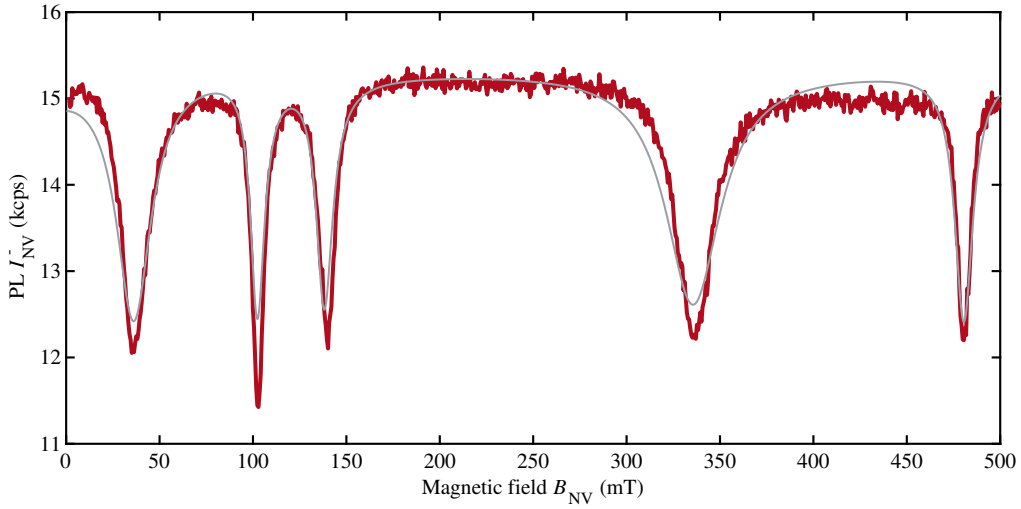


FIG. 5. NV^- photoluminescence (PL) signal, I^-_{PL}, as a function of magnetic field, B_{NV}, for NV1-S1. The fitting values are: $\delta_\perp = 4.444 \pm 0.003 GHz$, $\phi_\delta = -11.6 \pm 1.3°$, $g_l = 0.1395 \pm 0.0009$; B field misalignment: $\theta = 1.14 \pm 0.03°$; Excitation and scaling parameters: $\beta_{E_x} = 0.0221 \pm 0.0003$, $\beta_{E_y} = 0.0242 \pm 0.0005$, $I^-_{bck} = 4378 \pm 92$cps;

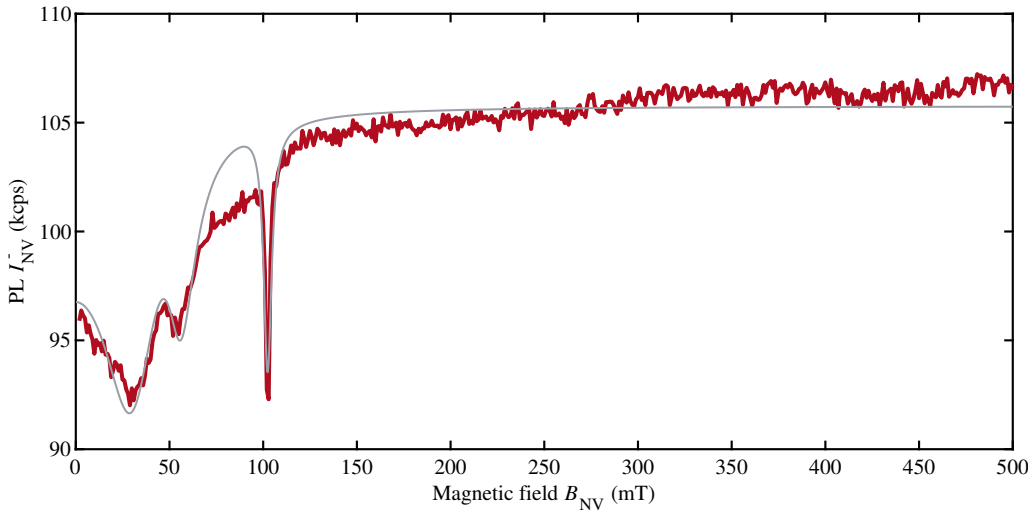


FIG. 6. NV^- photoluminescence (PL) signal, I^-_{PL}, as a function of magnetic field, B_{NV}, for NV2-S2. The fitting parameters are: $\delta_\perp = 38.6 \pm 0.7$GHz, $\phi_\delta = 1 \pm 59°$; B field misalignment: $\theta = 0.61 \pm 0.03°$; Excitation and scaling parameters: $\beta_{E_x} = 0.085 \pm 0.005$, $\beta_{E_y} = 0.186 \pm 0.014$, $I^-_{bck} = 70910.429 \pm 244.9818$cps;

Due to the new decay channels in the model also the NV^- PL needs to be rescaled when using the 12-level model. We found that merely with leaving the I^-_{PL} as a free parameter gives good accordance with the data. This leaves the fit to the NV^- PL with:

$$I^-_{PL} = f(I^-_{bck}) \tag{29}$$

where I^-_{bck} is the background counts in the wavelength spectrum of the collected NV^- PL.

The NV^0 PL exactly mirrors the dips of the NV^- with peaks. This behavior cannot be explained solely by the known ionization and recombination processes between the two charge states. Considering only them would lead to the same dips as there are in the NV^- PL instead of the observed peaks. However when introducing the recently proposed channel from the NV^- singlet to the NV^0 ground state this behavior can be explained with our model. Even when leaving more free fit parameters, without a certain minimal value for the shelf-ionization rate the behavior of the data cannot be reproduced. The fits produce a larger value of background fluorescence counts in the fitting

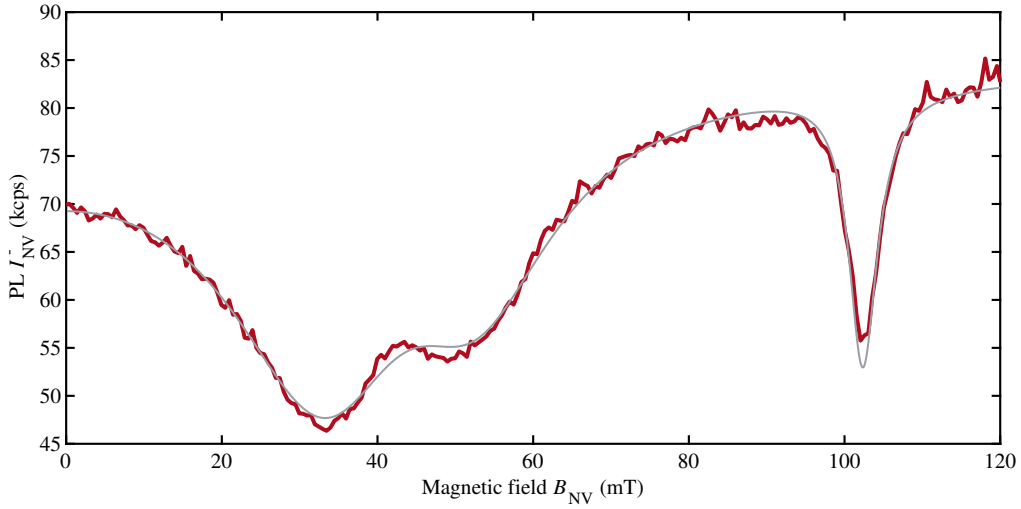


FIG. 7. NV^- photoluminescence (PL) signal, I^-_{PL}, as a function of magnetic field, B_{NV}, for NV3-S2. The fitting parameters are: $\delta_\perp = 55.9 \pm 0.6$GHz, $\phi_\delta = -32.2 \pm 0.6^\circ$; B field misalignment: $\theta = 0.502 \pm 0.010^\circ$; Excitation and scaling parameters: $\beta_{E_x} = 0.240 \pm 0.006$, $\beta_{E_y} = 0.64 \pm 0.02$,, $I^-_{bck} = 9091 \pm 231$cps;

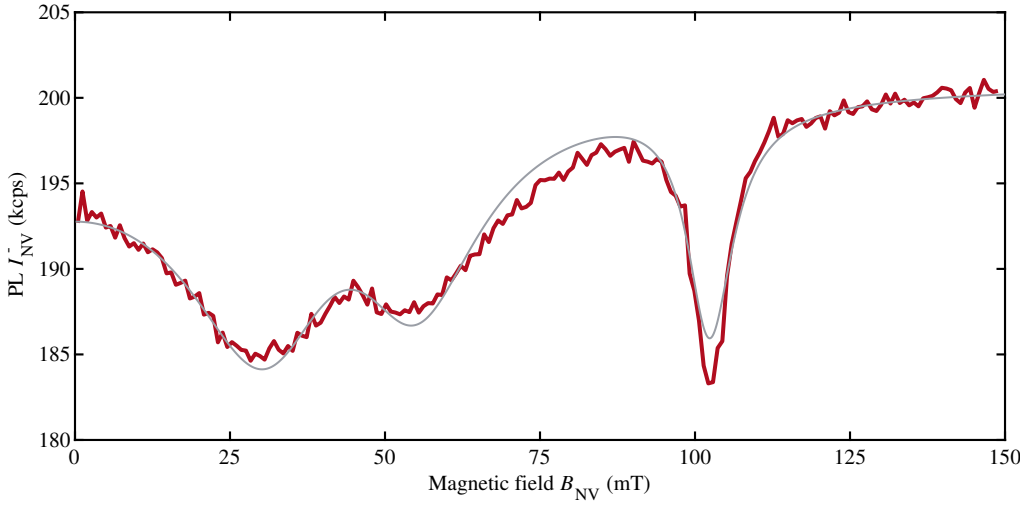


FIG. 8. NV^- photoluminescence (PL) signal, I^-_{PL}, as a function of magnetic field, B_{NV}, for NV4-S3. The fitting parameters are: $\delta_\perp = 42.3 \pm 0.5$GHz, $\phi_\delta = -26 \pm 2^\circ$; B field misalignment: $\theta = 1.06 \pm 0.03^\circ$; Excitation and scaling parameters: $\beta_{E_x} = 0.102 \pm 0.003$, $\beta_{E_y} = 0.164 \pm 0.007$, $I^-_{bck} = 158011 \pm 234$cps;

values of the NV^- data. This increase could indicate some small discrepancy with the ionization, recombination and shelf-ionization rates and/or their dependence on laser power.

NV-Sample	η_{NV^0}	I^0_{bck} (cps)	I^-_{bck} (cps)
NV1-S1	0.00132(3)	1258(11)	7980(8)
NV2-S2	0.001820(7)	7963(10)	79176(52)

TABLE IV. Summary of the fit results of the I^0_{PL} and I^-_{PL} spectra.

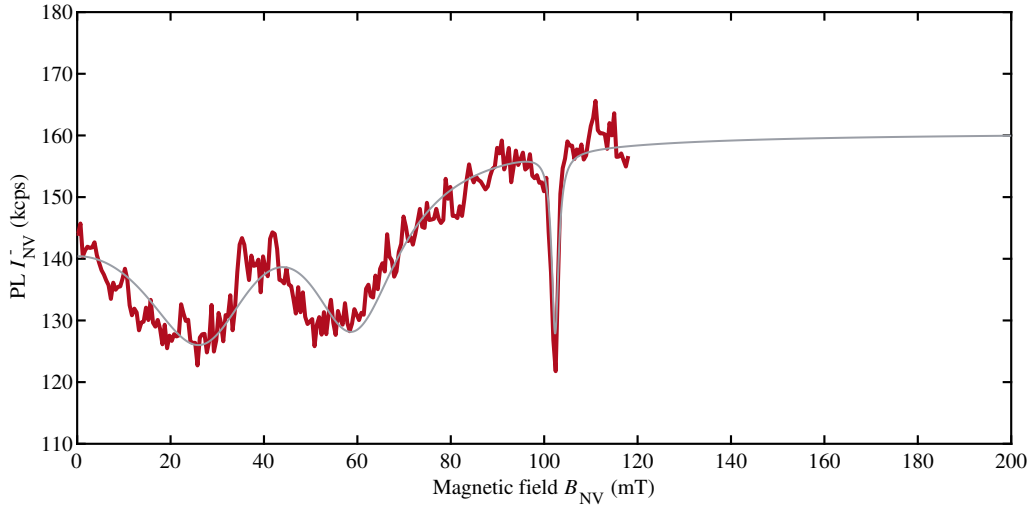


FIG. 9. NV^- photoluminescence (PL) signal, I^-_{PL}, as a function of magnetic field, B_{NV}, for NV5-S2. The fitting parameters are: $\delta_\perp = 32.0 \pm 0.5$ GHz, $\phi_\delta = -29 \pm 3°$; B field misalignment: $\theta = 0.20 \pm 0.02°$; Excitation and scaling parameters: $\beta_{E_x} = 0.43 \pm 0.03$, $\beta_{E_y} = 0.52 \pm 0.05$, $I^-_{bck} = 83198 \pm 883$ cps; The strain values are used to calculate the ESR contrast and the sensitivity in Fig. 4. The scaling parameters have been adapted due to the different laser power during the ESR experiment.

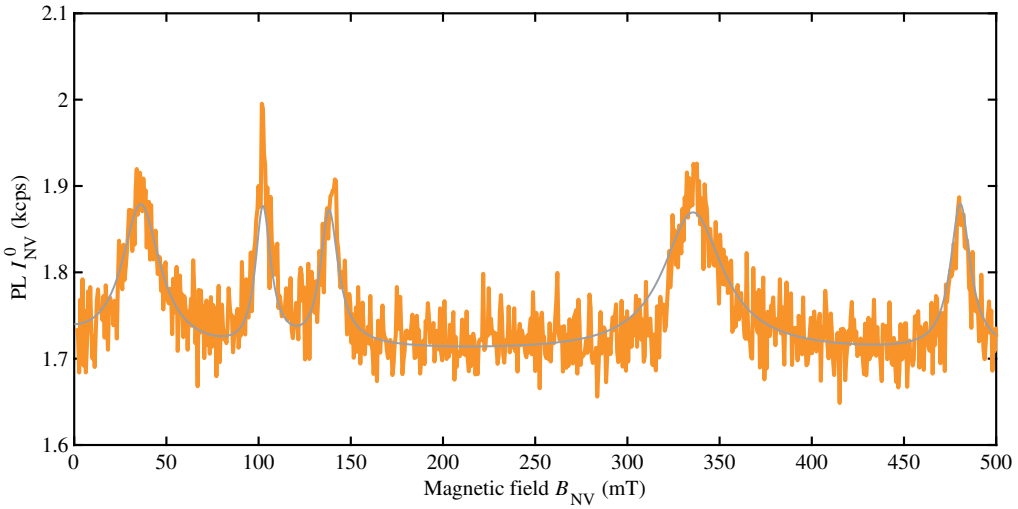


FIG. 10. NV^- photoluminescence (PL) signal, I^0_{PL}, as a function of magnetic field, B_{NV}, for NV1-S1. The fitting values for NV^0 and NV^- PL are: $\eta_{NV^0} = 0.00132 \pm 0.00003$ and the background fluorescence for NV^0 $I^0_{bck} = 1258 \pm 11$; the background fluorescence for NV^- $I^-_{bck} = 7980 \pm 8$;

Experimental details

Experimental apparatus

The NV experiments are performed in a closed-cycle refrigerator (Leiden Cryogenics, CF-CS81) with a $(B_x, B_y, B_z) = (1, 1, 5)$ T vector magnet. All of the measurements were all performed at a temperature of around 4 K. The cryostat possesses free-space optical access allowing the optical initialization and read-out of the NV through a confocal microscope with a green excitation laser at 532 nm (Coherent Compass 315M), where the excitation polarization is controlled with a liquid crystal polarization rotator (Thorlabs LCR-532). The NV PL read-out is performed with an avalanche photo-diode (Excelitas SPCM-AQRH-33) with a 650 nm long-pass filter (Thorlabs FELH0650) for the NV^- or a 600/52 nm bandpass filter (Semrock FF01-600/52-25) for the NV^0. An example of these filters on a diamond nanopillar can be seen in Figure 12. The NV spectrum is obtained with a spectrograph (Princeton Instruments,

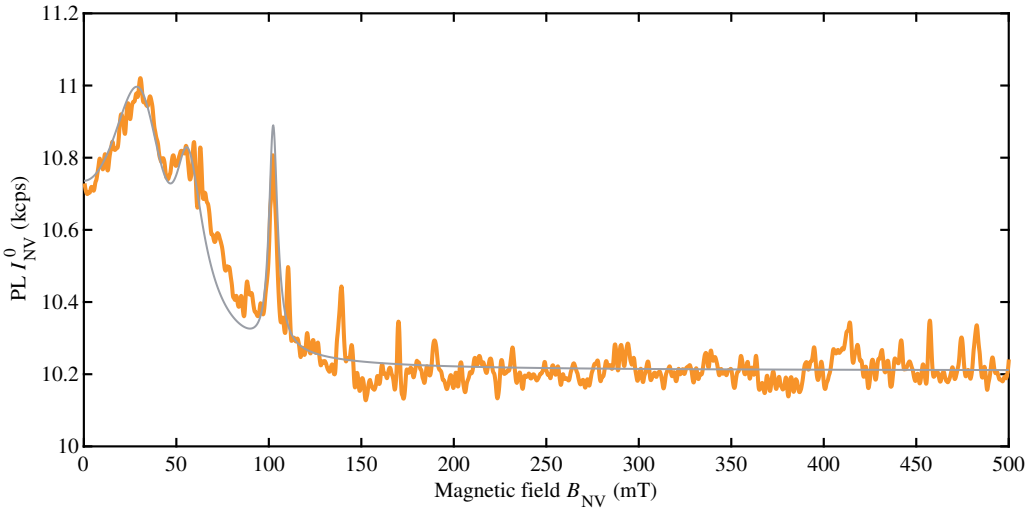


FIG. 11. NV^- photoluminescence (PL) signal, I^0_{PL}, as a function of magnetic field, B_{NV}, for NV2-S2. The fitting values for NV^0 and NV^- PL are: $\eta_{NV^0} = 0.001820 \pm 0.000007$ and the background fluorescence for NV^0 $I^0_{bck} = 7963 \pm 10$; the background fluorescence for NV^- $I^-_{bck} = 79176 \pm 52$;

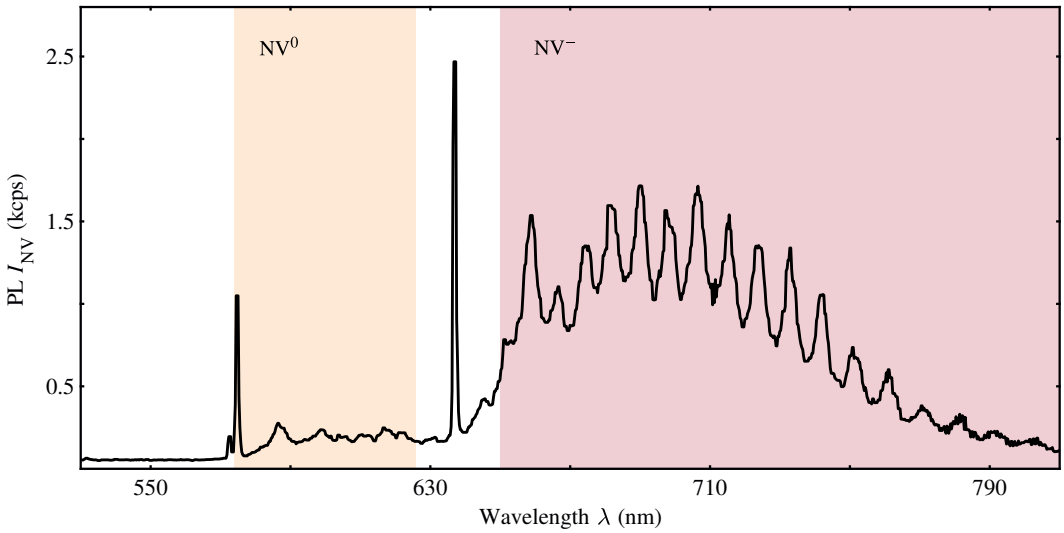


FIG. 12. Optical emission spectrum of a single NV in a diamond nanostructure[22, 24]. The highlighted regions indicate the regions of collected PL to separate the slightly overlapping spectra of the charge states NV^0 (orange) and NV^-(red).

HRS-500) and imaged with a low-noise camera (PIXIS 100).

The microwave control of the NV spin was performed using a constant microwave driving field from a signal generator (SRS SG384) that was modulated via an IQ-modulator (Polyphase microwave, AM0350A Quadrature Modulator) and an AWG (Spectrum generator NETBOX DN2.663-04). The microwave are then applied to the NV spin via a 25 μm thick Al wire that the NV is brought into close proximity with. The NV photoluminescence is then measured via gating the output of the APD with a TTL-router (in-house built, SP995) which is controlled via the AWG and whose output is measured with a DAQ (NI PXIE-1073, PXI-6220).

Samples details

In the following, we provide additional details on the samples used in this work:

Sample S1 is identical to the sample used in ref. [23], where extensive details on the sample and sample fabrication are given. The sample is a (100)−oriented, chemical vapor deposition (CVD) grown type IIa "electronic grade"

diamond from Element 6. Solid immersion lenses were fabricated by focused ion beam milling around pre-localized, naturally occurring NV centers located $5-15$ μm below the sample surface.

Sample S2 consisted of a commercially available, (100)−oriented, CVD grown type IIa "electronic grade" diamond from Element 6. NV centers were created by $^{14}N^{+}$ ion implantation at 12 keV and subsequent annealing as described elsewhere [44]. This procedure results in NV centers located ~ 10 nm from the diamond surface. To increase photon collection efficiency from the NVs, cylindrical diamond nanopillars of ~ 200 nm diameter were fabricated in the sample surface [44]. The sample fabrication procedure was tailored to yield an average of one NV center per diamond pillar.

Sample S3: is identical to the sample used in ref. [29], where extensive details on the sample and sample fabrication are given. The sample was CVD grown by the group of J. Achard and A. Tallaire with methods described in detail in Ref. [45]. NV centers were created in growth through controlled incorporation of N gas into the growth reactor. Under the growth conditions used here, these leads to NV centers whose quantization axis is preferentially aligned with the 111 growth direction and which typically show excellent spin properties [46]. We note that the sample exhibits elevated fluorescence background levels from SiV centers which were inadvertedly introduced during sample growth.

Prior to our experiments, samples S2 and S3 were acid cleaned using a well-established acid cleaning technique, details in Ref. [47]. This sample cleaning method leaves the diamond surface predominantly O-terminated. No acid cleaning was employed for sample S1 to preserve pre-existing antenna structures on the sample surface. Given the micron-scale depth of the NVs examined in sample S1, sample cleaning and surface termination are or minor relevance to the behavior of NVs studies in this sample.

g_l factor measurements

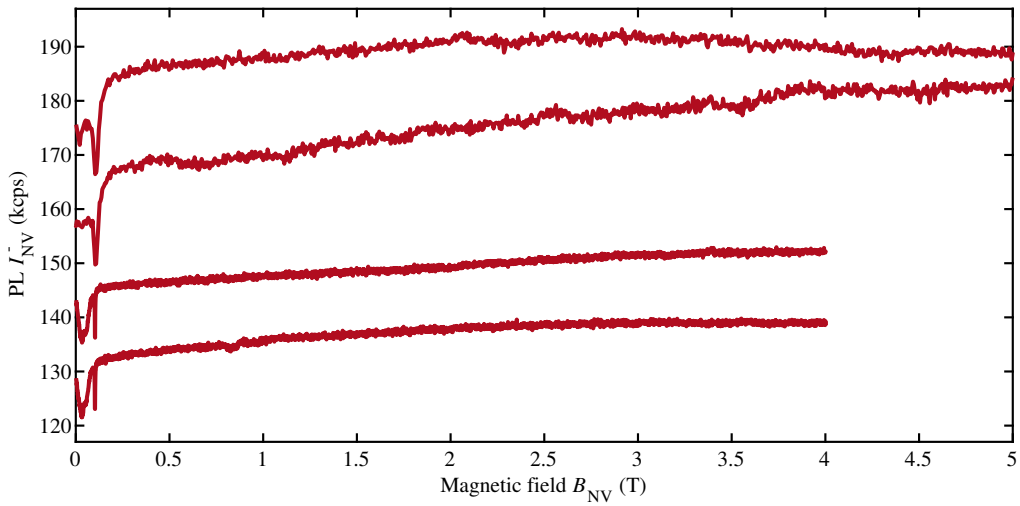


FIG. 13. NV^{-} photoluminescence (PL) signal, I_{PL}^{-} as a function of magnetic field, B_{NV}, for multiple NVs showed with an offset. According to our model all of the shown NV PL spectra should show PL dips in the shown magnetic field range. They are exemplary and show full field scans. Most of the performed scans were regions of magnetic field investigating of various parts of the magnetic field. To determine the strain appropriately we performed high resolution scans at low magnetic fields.

For the measurement of the inter-branch level anti crossings $E_{x(y)} \leftrightarrow E_{y(x)}$ at high magnetic fields, the 111 oriented sample S3 was introduced to maximize the magnitude of B_{NV} that we could access in our experimental setup equipped with a 1T/1T/5T vector magnet. With all NVs, we proceeded as described for NV4-S3 in the main text: We first characterized NVs with PL versus B measurements al "low" magnetic fields (c.f. Fig.2a in the main text) to determine the effective strain parameter. After that we investigated $I_{PL}^{-}(B_{NV})$ for B_{NV} up to 5 T. Due to slow magnetic field ramp speeds and occasional signal drifts, we mostly performed magnetic field sweeps over smaller intervals in B_{NV}, and only few measurements cover the entire range – those data are shown in Fig. 13. Some of the data include a low-frequency envelope, which results from system drifts during the magnetic field sweeps. The NVs we investigated in S3 all showed $\delta_{\perp}$-values on the range 30...50 GHz. According to our model, these NVs should all exhibit their $E_{x(y)} \leftrightarrow E_{y(x)}$ inter-branch ESLACs, and a corresponding I_{PL}^{-} drop, in the centre of the magnetic field sweep range shown in Fig. 13, unless g_l is significantly enhances, as discussed in the main text.

Magnetic field sensitivity

In order to probe the effect of the excited state level anticrossings on the performance of magnetic field sensing, single NV spins in nanopillars (Sample S2) were brought into close proximity (within 100 μm) of a 25 μm thick Al wire. To remove frequency dependent performance of the microwave circuitry, at each magnetic field position RABI measurements were performed to tune the microwave driving power to maintain an average π-time of 200 ns (power broadened, results shown in main script) and 1 μs (hyperfine resolved). The optically detected magnetic field measurements where then performed with a standard pulsed ODMR technique [13] with these driving times and fitted with Lorentzian functions.

We were not able to detect any statistically difference in the variation in sensitivity between the power broadened and hyperfine resolved ODMR. Additionally, we did not observe any additional effect on the nuclear spin polarization, which is starkly different to the room temperature excited state level anticrossing, where polarization of greater than 90% have been observed [48].

To compare the sensitivity and contrast with the model, we first fit the NV$^-$ I_{PL} spectra to obtain the parameters from the model. These fit parameters are then used to predict the contrast of the ODMR as a function of magnetic field, $\mathcal{C}(B)$. The combination of the fitted $I^0_{\mathrm{PL}}(B)$ and the predicted $\mathcal{C}(B)$ are then used in conjunction with the average ODMR width (small variation due to rabi tuning) to predict the sensitivity, $\eta(B)$.

Polarization dependence of the NV PL

The optically pumping to the excited state orbital doublet has a polarization dependence. Therefore it is possible to control the prominence of the dips in the PL which arise due to level anticrossing. The control is limited due to the non-radiative relaxation after pumping [15].

Here we controlled the rotation of the 532nm excitation via a liquid crystal rotator with a 1000:1 extinction ratio which was placed after the dichroic mirror before the objective.

In both the higher (Fig. 14) and low stress regime (Fig. 15) we found that we could change the contrast of the peaks.While this is not a significant amount of tuning, it is possible that further tuning is possible through changing the wavelength of the excitation as well as further optimization of the polarization control.

The NV^0 PL also shows a dependence on the laser polarization which can be seen in the upper part of Fig. 15.

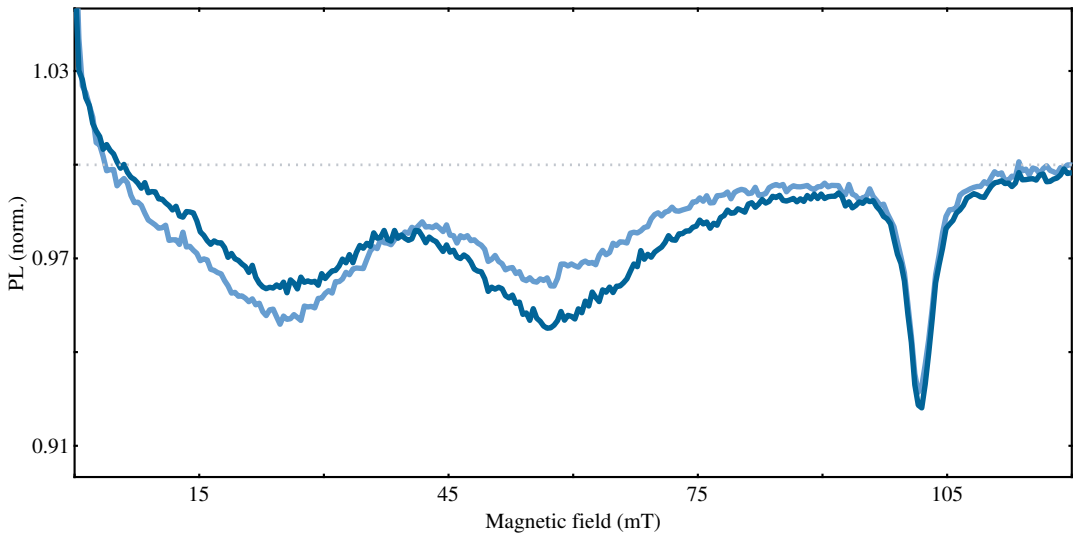


FIG. 14. Normalized NV$^-$ photoluminescence (PL) signal, I^-_{PL}, as a function of magnetic field, B_{NV}, for two orthogonal laser polarizations of an NV in S3. The two inter-branch LAC are well resolved. The initial drop in counts is attributed to a nearby NV which is quenched with magnetic field.

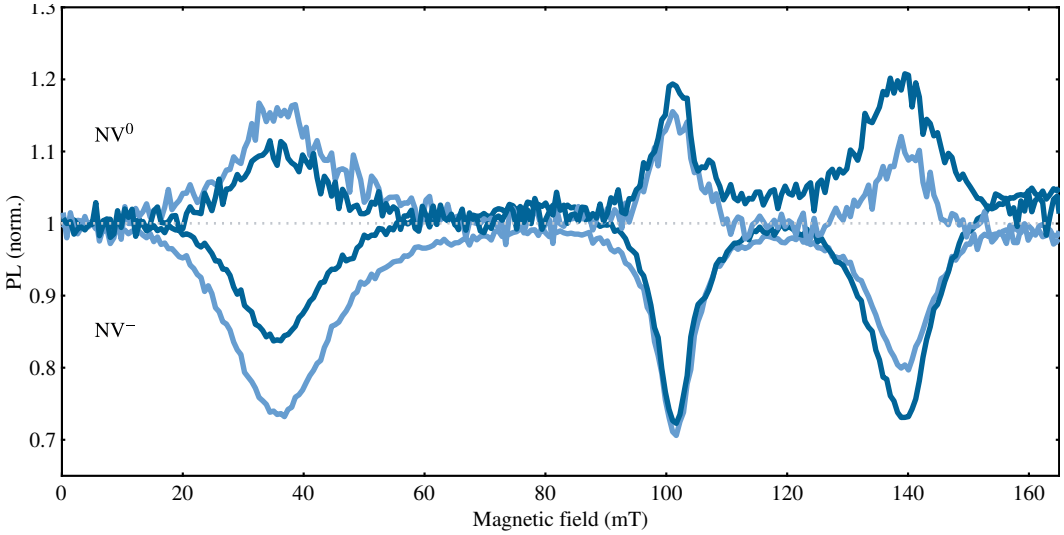


FIG. 15. Normalized NV^- photoluminescence (PL) signal, I^-_{PL}, and normalized NV^0 photoluminescence (PL) signal, I^0_{PL}, as a function of magnetic field, B_{NV}, for the low-strain NV1-S1. Two orthogonal laser polarizations have been used. The NV^0 signal shows a dependence on laser polarization at the same positions as the NV^- does. When the NV^- countrate decreases at an ES LAC, the corresponding NV^0 countrate increases and vice versa.